Tellus (1997), 49A, 544–558
Printed in UK – all rights reserved

TELLUS
ISSN 0280–6495

Interannual variation of atmospheric mass and the southern oscillation

ByTSING-CHANG CHEN[1]*, JAU-MING CHEN[1] AND SIEGFRIED SCHUBERT[2] *Atmospheric Science Program, Department of [1]Geological and Atmospheric Sciences, Iowa State University, Ames, Iowa, USA, and [2]Data Assimilation Office, Laboratory for Atmospheres, Goddard Space Flight Center/NASA, Greenbelt, MD, USA*

(Manuscript received 14 October 1996; in final form 7 July 1997)

ABSTRACT

Two reanalysis datasets, one generated by the Goddard Laboratory for Atmospheres for 1982–1993 and the other generated by the National Centers for Environmental Prediction for 1982–1995, are used to examine the relationship between the Southern Oscillation (SO) and the interannual variation of atmospheric mass. Both reanalyses show that atmospheric mass increases (decreases) during the positive (negative) SO phase. Atmospheric mass consists of dry air and moisture. Since dry mass is conserved, the interannual variation of atmospheric mass results from the variation of water vapor pressure. Thus, global atmospheric hydrological processes are analyzed to illustrate how the SO affects the interannual variation of atmospheric mass. During the positive (negative) SO phase, water vapor is converged (diverged) toward (out of) the central-eastern tropical Pacific [where sea surface temperatures (SSTs) are higher (lower) than normal] to maintain (suppress) cumulus convection in that area. An anomalous east-west Walker circulation straddling the Dateline is driven by the anomalous cumulus convection in this region to create positive (negative) surface pressure anomalies over the western tropical Pacific-Indian Ocean, which result in an increase (decrease) in atmospheric mass.

1. Introduction

The southern oscillation (SO) (Walker 1923, 1924, 1928; Walker and Bliss 1930, 1932, 1937) is an interannual seesaw in surface pressure (and thus in *atmospheric mass*) between the tropical Indian-western Pacific Ocean and most of the tropical Pacific. The spatial structure of the SO is often depicted in terms of the global correlation coefficient pattern between the surface pressure anomalies and surface pressure anomalies at an observational station close to the center of an SO cell, employing as base points, e.g., Djakarta, Indonesia (Berlage 1957) and Darwin, Australia (Trenberth and Shea 1987). Because surface pressure exhibits a seesaw between the two sides of the Pacific following the SO, the surface pressure difference between Tahiti (near the center of the eastern SO cell) and Darwin (close to the center of the western SO cell) has been adopted by the climate research community as the Southern Oscillation Index (SOI, W. Chen 1982) to indicate the temporal evolution of this low-frequency climate mode.

The total atmospheric mass is measured by the globally-integrated surface pressure. It is thus likely that the SO signal exists in atmospheric mass following the SO seesaw in surface pressure. Trenberth et al. (1987) analyzed the interannual

* Corresponding author.
Address: Atmospheric Science Program, 3010 Agronomy Hall, Department of Geological and Atmospheric Sciences, Iowa State University, Ames, IA 50011.
e-mail tmchen@iastate.edu

variation of atmospheric mass with the data generated by the Global Data Assimilation System (GDAS) of the European Centre for Medium Range Weather Forecasts (ECMWF) for 1978–1985. Although a warm (1982/83 winter) and a cold (1984/85 winter) El Niño-Southern Oscillation (ENSO) event occurred during this time period, the SO signal was not clearly revealed by Trenberth et al.'s (loc. cit.) analysis. This lack of a signal may be attributed to the substantial changes and updates in the operational ECMWF GDAS (Trenberth and Olson 1988). Apparently, a uniformly assimilated dataset of surface pressures over a long time period is required in order to examine the interannual variation of atmospheric mass.

According to the surface pressure tendency equation, surface pressure change is determined by the convergence of mass into a vertical column of atmosphere (Van den Dool and Saha 1993), a result of atmospheric mass redistribution. The interannual variation of atmospheric mass is presumably coupled with the SO seesaw in surface pressure and with that of the global divergent circulation linked to the SO. The divergent circulation portrayed by GDAS data is generally sensitive to the particular data assimilation system being employed. Changes in assimilation systems make it difficult, if not impossible, to use the GDAS data of any operational center over the past one-and-a-half decades to depict reliably the interannual variation of the global divergent circulation. Atmospheric mass consists of dry air and moisture. Since dry atmospheric mass is conserved, the seasonal variation of atmospheric mass results from the variation of precipitable water (Trenberth et al. 1987, Van den Dool and Saha 1993, Chen et al. 1996b). The goal of this study is to explore the cause of the interannual variation of atmospheric mass. One may question whether the interannual variation of precipitable water plays a vital role in this variation. The lack of dynamical constraints and the spinup problems of a GDAS may make it difficult to answer this question because the assimilated precipitable water may contain the GDAS model bias. Thus, in addition to comparing results from more than one data assimilation system, it may be of use to verify our analysis of precipitable water with a water vapor dataset independent of the model bias.

The reanalysis data generated by Version 1 of the Goddard Earth Observing System (GEOS) data assimilation system (DAS) (Schubert et al. 1993) and the GDAS of the National Centers for Environmental Prediction (NCEP) (Kalnay and Jenne 1991, Kalnay et al. 1996) became available recently. Because of the uniformity in each aforementioned assimilation dataset, we shall use the 1982–1993 GEOS data and the 1982–1995 NCEP data to demonstrate in Section 2 a possible link between the interannual variation of atmospheric mass and the SO seesaw in surface pressure. A possible coupling between the SO seesaw in surface pressure and the global divergent circulation is illustrated in Section 3. The interannual variation of some atmospheric hydrological processes related to interannual variation of atmospheric mass is presented in Section 4. Both a brief comparison between the two assimilation systems and a comprehensive comparison between hydrological processes depicted by the two datasets were made by Mo and Higgins (1996). The hydrological variables of each dataset may contain the assimilation system bias. Thus, the 1987–1992 precipitable water and the 1982–1994 precipitation data generated under the NASA Water Vapor Project (NVAP; Randal et al. 1995) and the NOAA Global Precipitation Climatology Project (GPCP) of the Climate Prediction Center (CPC) (Xie and Arkin 1997), respectively, are also analyzed to verify and assess interannual variation in the water vapor pressure and precipitation of the assimilation datasets. Concluding remarks are made in Section 5.

2. Interannual variation of atmospheric mass

The temporal variation of the monthly-mean surface pressure (p_s) averaged globally is dominated by annual and semiannual cycles. Thus, we isolate the interannual variations of p_s by a second-order Butterworth lowpass filter with a high-frequency cutoff at 18 months (Chen et al. 1996a). In what follows, a globally-averaged variable ( ) is denoted by [( )], and the lowpass filtered variable ( ) by $(\tilde{\ })$. Displayed in Fig. 1 are time series of $[\tilde{p}_s]$(GEOS) and $[\tilde{p}_s]$(NCEP). As revealed from the spatially-averaged departure of sea-surface temperature (SST) from its long-term mean, over the NINO-3 region (150°–90°W, 5°S–5°N), two cold (1984/85 and 1988/89 winters)

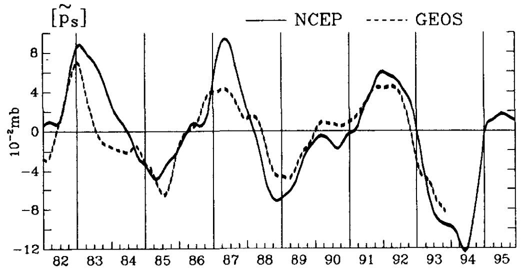

Fig. 1. Time series of the globally-averaged low-pass filtered (with a 18-month cut-off time) surface pressure, $[\tilde{p}_s]$·$[\tilde{p}_s]$ computed with the GEOS-DAS data is denoted by a dashed line, while that computed with the NCEP-GDAS data is shown by solid line.

and three warm (1982/83, 1986/87 and 1991/92 winters) ENSO events are covered by the two assimilation datasets used in this study. Since the time period of available data is so short, the end effect of the low-pass filtering may affect the beginning and end of the $[\tilde{p}_s]$ time series. Regardless of this end effect, the interannual variation signal of $[\tilde{p}_s]$ is coincident with the ENSO activity. In particular, $[\tilde{p}_s]$ exhibits a positive (negative) maximum during warm (cold) ENSO events. Since atmospheric mass is proportional to p_s, the interannual variation of $[\tilde{p}_s]$ shown in Fig. 1 reveals that atmospheric mass increases (decreases) during the positive (negative) SO phase. The difference in $[\tilde{p}_s]$ between positive and negative events is about 0.1 mb, which is smaller than the difference between the summer minimum and winter maximum of $[p_s]$ ($\sim$0.5 mb) (e.g. Chen et al. 1996b). However, the coincidence between interannual variation in $[\tilde{p}_s]$ and the ENSO activity is unlikely to be accidental. Next, we examine further the relationship between the interannual variation in $[\tilde{p}_s]$ and the SO.

The relationship between the interannual variation in atmospheric mass and the SO is inferred from the local correlation between $[\tilde{p}_s]$ and $\tilde{p}_s$, denoted by $\sigma_{[\tilde{p}_s]\cdot\tilde{p}_s}$. Shown in Fig. 2 is $\sigma_{[\tilde{p}_s]\cdot\tilde{p}_s}$ computed with both the GEOS and NCEP data. In the tropical-subtropical region, the positive and negative values of $\sigma_{[\tilde{p}_s]\cdot\tilde{p}_s}$ are more or less separated by the Dateline. In view of the alternation of $[\tilde{p}_s]$ between the positive and negative SO phases, $\sigma_{[\tilde{p}_s]\cdot\tilde{p}_s}$ reveals a seesaw of $\tilde{p}_s$ on the two sides of the Dateline. Also discernible is a teleconnection wave train extending from the western tropical Pacific to the middle-high latitudes of each hemisphere; these resemble the Pacific-North American (PNA) (Wallace and Gutzler 1981) and Pacific-South American (PSA) (Mo and Ghil 1987, Karoly 1989) patterns. The overall $\sigma_{[\tilde{p}_s]\cdot\tilde{p}_s}$ pattern resembles Trenberth and Shea (1987) with Darwin surface pressure as a base point.

While Fig. 2 shows the phase relationship between the interannual variation of atmospheric mass and the SO, it does not provide information about the local amplitude of interannual variation in p_s. To accomplish this we select a positive SO phase (86/87 winter) and a negative SO phase (88/89 winter) with the GEOS-DAS $\tilde{p}_s$ for illustration (Fig. 3). Recall that the large-scale perturbation of surface pressure in the tropics is an order of magnitude smaller than that in mid-latitudes (Holton 1992). As shown in Fig. 3, this is true also for the interannual variation of surface pressure: the maximum local amplitude of $\tilde{p}_s$ is about 1 mb in the tropics, while it is about 3 mb in midlatitudes. The small value of $[\tilde{p}_s]$ results from the cancellation between positive and negative values of $[\tilde{p}_s]$.

Based upon the contrast between the $[\tilde{p}_s]$ time series (Fig. 1) and the spatial structure of the $\sigma_{[\tilde{p}_s]\cdot\tilde{p}_s}$ (Fig. 2) pattern, we conclude that atmospheric mass (indicated by $[\tilde{p}_s]$) increases (decreases) during a positive (negative) phase of the SO; i.e., during a warm (cold) ENSO event, with a positive (negative) $\tilde{p}_s$ anomaly west of the Dateline and a negative (positive) $\tilde{p}_s$, anomaly east of the Dateline.

3. Interannual variation of the global divergent circulation

It was pointed out in the Introduction that surface pressure change is caused by convergence of air mass into a vertical column. The SO seesaw of surface pressure (or atmospheric mass) may be attributed to the redistribution of atmospheric mass, which is induced by the interannual variation of the global divergent circulation in response to the anomalous SST forcing in the Pacific. In order to gain a simultaneous global view of the interannual variation in the global divergent circulation and interannual variations of both $[\tilde{p}_s]$ and $\tilde{p}_s$, we perform empirical orthogonal function (EOF) analyses of $\tilde{\chi}$(200 mb), $\tilde{\chi}$(850

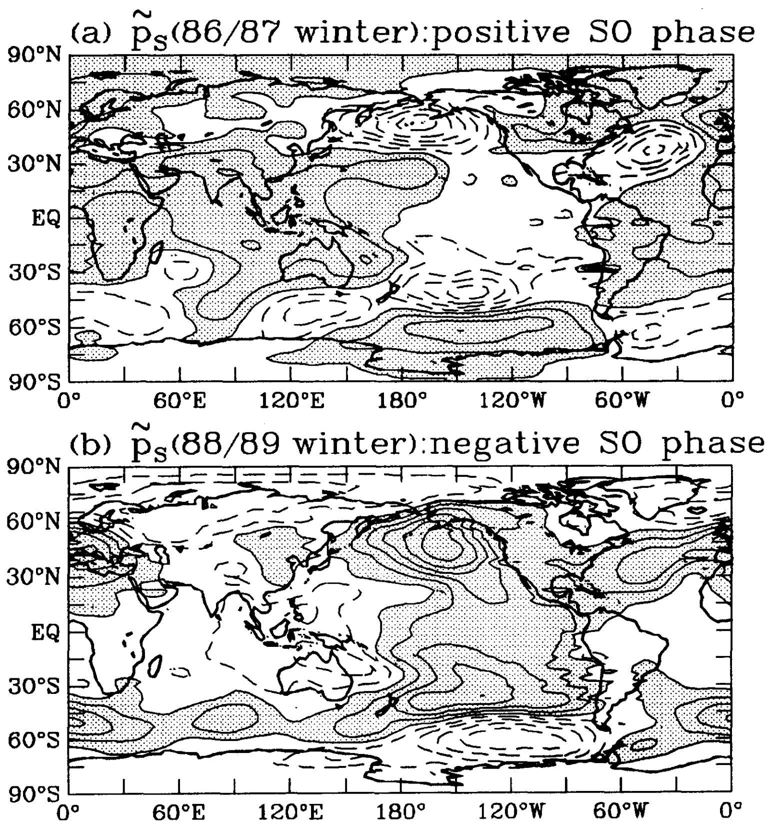

Fig. 2. Distribution of the correlation coefficients between $[\tilde{p}_s]$ and $\tilde{p}_s$ anomalies over the globe with (a) the GEOS-DAS data and (b) the NCEP-GDAS data. Positive (negative) values of $\sigma_{[\tilde{p}_s]\cdot\tilde{p}_s}$ are contoured with solid (dashed) lines with a contour interval of 0.2. The positive value of $\sigma_{[\tilde{p}_s]\cdot\tilde{p}_s}$ is stippled.

mb), $\tilde{\psi}_m$ and $\tilde{p}_s$. The velocity potential (χ) analyzed here is obtained by solving the Poisson equation (with horizontal divergence) through the spherical harmonic method and through a triangle truncation at 31 waves. The mass flux function ψ_m is computed by a simple diagnostic approach described in the Appendix.

Figs. 4 and 5 show the eigencoefficient (C1) time series and eigenvector (E1), respectively, of the first eigenmode derived from the four aforementioned variables. The percentage shown on each panel of Fig. 4 is the total variance explained by the first eigenmode of each variable. Results of the EOF analyses are as follows.

(1) There are some differences between the 2 data sets in the time periods and the total variances explained by the corresponding first eigenmodes. However, the temporal variations of the C1 time series and the E1 spatial structures in the 2 data sets agree highly.

(2) C1 time series of all four variables are coherent not only with themselves, but also with the $[\tilde{p}_s]$ time series. Correlations between $[\tilde{p}_s]$ time series and C1 time series of $\tilde{\chi}$(200 mb), $\tilde{\chi}$(850 mb) and $\tilde{\psi}_m$ range between 0.75 and 0.9. Apparently, the interannual variation of atmospheric mass coincides with that of the global divergent circulation.

(3) Horizontal divergence of large-scale tropical motion reverses once vertically in the troposphere. Thus, it is not surprising to see that E1[$\tilde{\chi}$(200 mb)] and E1[$\tilde{\chi}$(850 mb)] are *opposite* in their spatial structure. In addition to the vertical reversal in their horizontal structure, these two eigenvectors are horizontally out of phase with their corresponding annual-mean velocity poten-

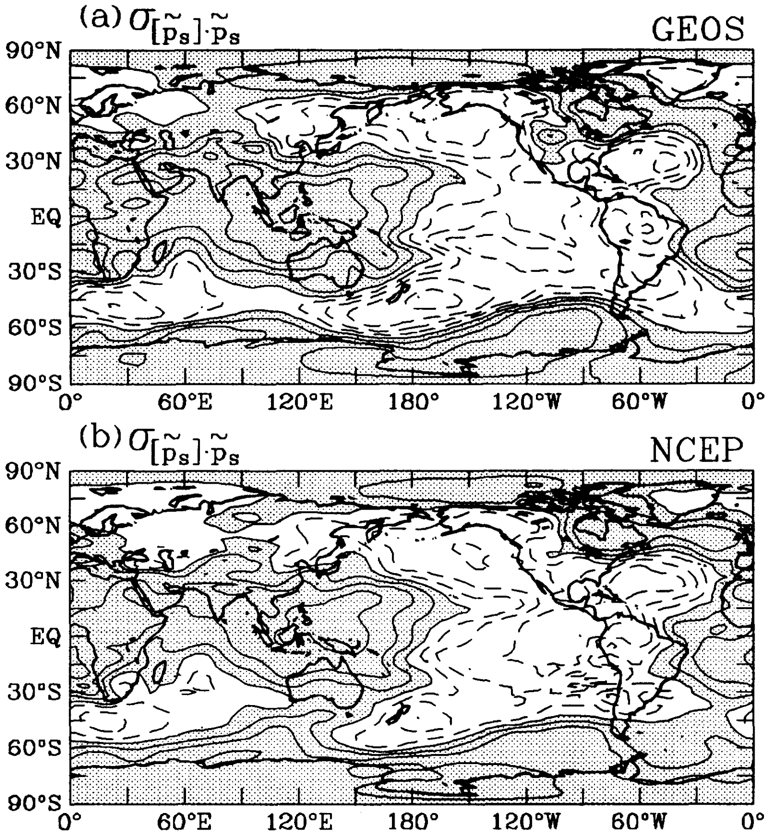

Fig. 3. Distribution of the GEOS-DAS $\tilde{p}_s$ anomalies averaged over (a) 1986/87 winter (December–February) and (b) 1988/89 winter. Positive (negative) values of $\tilde{p}_s$ are contoured with solid (dashed) lines with a contour interval of 0.5 mb. The positive value of $\tilde{p}_s$ is stippled.

tial (not shown). Apparently, the global divergent circulation is weakened (intensified) during the positive (negative) SO phase.

(4) The interannual variation of the east-west Walker circulation at the Equator can be inferred from the first eigenmode of $\tilde{\psi}_m$ (Figs. 4c, 5c, g). $\mathrm{E1}(\tilde{\psi}_m)$ exhibits a wavenumber-2 structure, resembling that portrayed by Kousky et al. (1984). In particular, the most intense and well-organized cell of $\mathrm{E1}(\tilde{\psi}_m)$ straddles the Dateline, with two major centers of both $\mathrm{E1}[\tilde{\chi}(200\ \mathrm{mb})]$ and $\mathrm{E1}[\tilde{\chi}(850\ \mathrm{mb})]$ located over the western and eastern tropical Pacific, respectively. As inferred from this particular cell of $\mathrm{E1}(\tilde{\psi}_m)$, during the positive (negative) SO phase an upward (downward) branch exists around 120°W and a downward (upward) branch around 120°E in accord with the anomalous warming (cooling) over the eastern tropical Pacific and the anomalous cooling (warming) over the western tropical Pacific. The downward branch of the anomalous east-west Walker circulation maintains positive $\tilde{p}_s$ anomalies, while the upward branch of this circulation maintains negative $\tilde{p}_s$ anomalies.

(5) The spatial structure of $\mathrm{E1}(\tilde{p}_s)$ resembles that of $\sigma_{[\tilde{p}_s]\cdot\tilde{p}_s}$ (Fig. 2). A SO seesaw in $\tilde{p}_s$ is revealed clearly from $\mathrm{E1}(\tilde{p}_s)$ in the tropical-subtropical region between the two sides of the Dateline. The contrast between $\mathrm{E1}(\tilde{\psi}_m)$ and $\mathrm{E1}(\tilde{p}_s)$ shows that in the tropical-subtropical region the positive (negative) $\mathrm{E1}(\tilde{p}_s)$ anomalies over the Indian and Pacific Oceans are located underneath the downward (upward) branch of the anomalous east-west Walker circulation. The SO seesaw of surface

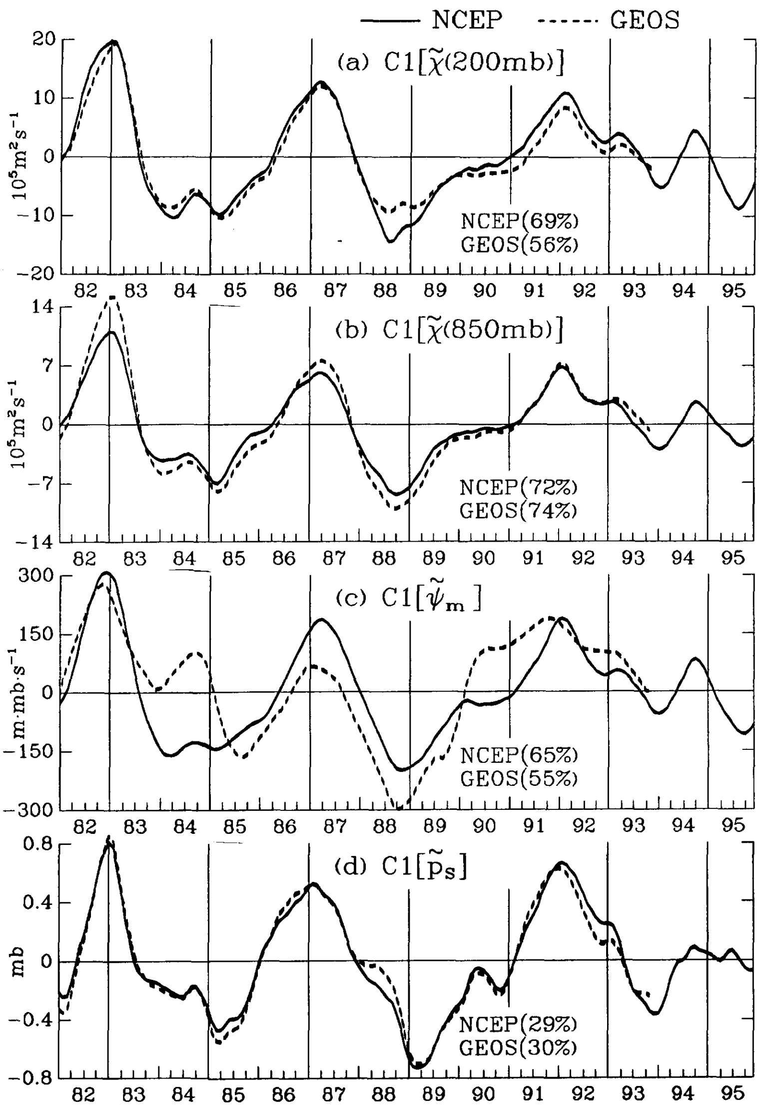

Fig. 4. Eigencoefficient time series of the first eigenmodes: (a) C1[$\tilde{\chi}$(200 mb)], (b) C1[$\tilde{\chi}$(850 mb)], (c) C1($\tilde{\psi}_m$] (d) C1($\tilde{p}_s$). The C1 time series generated with the GEOS-DAS data are denoted by dashed lines, while those generated with the NCEP-GDAS data are depicted by solid lines. The percent table shown on each panel is the total variance explained by the first eigenmode.

pressure in this region apparently follows the interannual variation of the east-west Walker circulation.

(6) The PNA and PSA teleconnection patterns stand out distinctly as E1($\tilde{p}_s$) anomalies in the Pacific-American longitudes. Although the local amplitude of $\tilde{p}_s$ is much larger in middle and high latitudes, the region between 30°S and 30°N occupies half of the global area. Thus, the SO of surface pressure in the tropical-subtropical region is a major contributor to the interannual variation of [$\tilde{p}_s$] shown in Fig. 1.

Finally, 2 comments should be made concerning

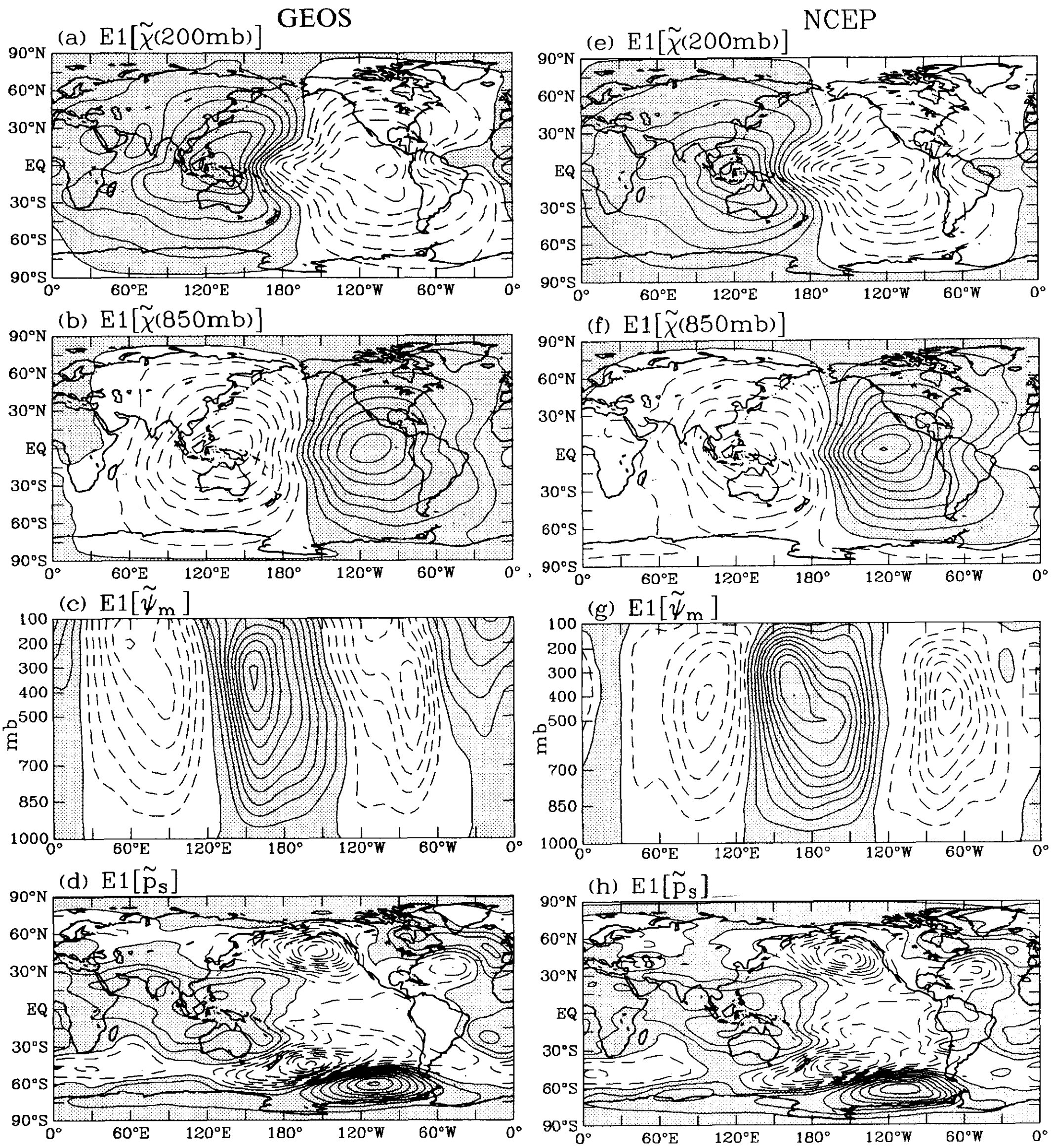

Fig. 5. Eigenvectors of the first eigenmodes generated with the GEOS-DAS data (in the left column) and with the NCEP-GDAS data (in the right column): (a) and (e) E1[$\tilde{\chi}$(200 mb)], (b) and (f) E1[$\tilde{\chi}$(850 mb)], (c) and (g) E1($\tilde{\psi}_m$) and (d) and (h) E1($\tilde{p}_s$). Positive (negative) values of E1 are contoured by a solid (dashed) line with a contour interval of 0.3 for (a), (b), (e) and (f), 0.1 for (c) and (g), and 0.4 for (d) and (h). The positive value of E1 is stippled.

our argument that the SO of surface pressure follows the interannual variation of the east-west Walker circulation.

(1) As speculated by Van den Dool and Saha (1993), the SO of surface pressure may be caused by the El Niño SST anomalies over the tropical Pacific. As we shall see, the adjustment process of surface pressure change is still accomplished by the east-west Walker circulation.

(2) The coupling between the interannual variation of the east-west Walker circulation and the

SO explains only the seesaw of surface pressure on the two sides of the Dateline. The increase and decrease of atmospheric mass following the positive and negative phase of the SO, respectively, are still not explained. This is the subject of the next section.

4. Interannual variation of hydrological processes

Atmospheric mass is comprised of dry and moist air, i.e., $p_s = p_d + p_w$, where p_d and p_s are surface pressures of dry air and water vapor, respectively. Since the mass of global dry air is conserved, the interannual variation of global-mean p_s should coincide with that of global-mean p_w, namely, $[\tilde{p}_s] = [\tilde{p}_w]$. To substantiate this argument for the assimilated data, time series of $[\tilde{p}_w]$ computed with the two datasets are displayed in Fig. 6. The amplitude of $[\tilde{p}_w]$(NCEP — solid line) is about a third to a half of the amplitude of $[\tilde{p}_s]$(NCEP) (Fig. 1). In contrast, the amplitude of $[\tilde{p}_w]$ (GOES — dashed line) varies from one-half to one amplitude of $[\tilde{p}_s]$(GEOS) (Fig. 1). The discrepancy between $[\tilde{p}_w]$ and $[\tilde{p}_s]$ is expected for the following reason: because the continuity equation of an assimilation system is dry, the only way by which the total atmospheric mass can change in the assimilation is from the analysis increments of sea-level pressure. Thus, there are no built-in constraints between the assimilation in moisture and total atmospheric mass. On the other hand, the correlation is about 0.85 between the $[\tilde{p}_w]$(GEOS) and $[\tilde{p}_s]$(GEOS) time series, and about 0.75 between the $[\tilde{p}_w]$(NCEP) and $[\tilde{p}_s]$(NCEP) time series. Apparently, interannual variations of $[\tilde{p}_w]$ and $[\tilde{p}_s]$ are more or less in phase.

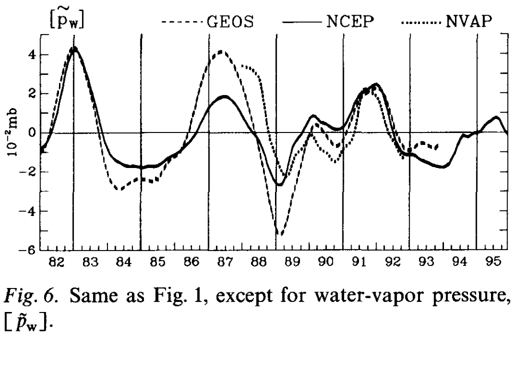

Fig. 6. Same as Fig. 1, except for water-vapor pressure, $[\tilde{p}_w]$.

By taking the assimilation system bias into account, the comparison between $[\tilde{p}_w]$ and $[\tilde{p}_w]$ time series supports the argument that the interannual variation of $[\tilde{p}_s]$ in the assimilation datasets is contributed by $[\tilde{p}_w]$. If the data assimilation system were perfect, interannual variations in $[\tilde{p}_w]$ and $[\tilde{p}_s]$ should be coincident not only in time, but also in their amplitude. With possible system biases, it is unlikely that both the GEOS and NCEP datasets can satisfy this perfect condition. Thus, we may wonder whether the actual interannual variation signals of water vapor pressure are not fully reflected by the $[\tilde{p}_w]$(GEOS) and $[\tilde{p}_w]$(NCEP) time series. In order to clarify this, the time series of $[\tilde{p}_w]$(NVAP) is shown in Fig. 6 for comparison. Regardless of its short period of coverage (1987–1992), the NVAP moisture dataset includes a cold (1988/89) and a minor warm (1991/92) ENSO event. The temporal variation of $[\tilde{p}_w]$(NVAP) in relative agreement with those of $[\tilde{p}_w]$(GEOS) and $[\tilde{p}_w]$(NCEP), although the amplitude of $[\tilde{p}_w]$(NVAP) is close only to that of $[\tilde{p}_w]$(NCEP). This comparison suggests that the two assimilation datasets contain to some extent the interannual variation component of water vapor pressure.

Recall that the interannual variation of $[\tilde{p}_s]$ results primarily from the SO of p_s in the Pacific-Indian Ocean basin. However, in view of the coherent variation of the $[\tilde{p}_s]$ (Fig. 1) and $[\tilde{p}_w]$ (Fig. 6) time series, the following 2 questions are raised.

(1) Is there a spatial oscillation of $\tilde{p}_w$ coherent with the east-west seesaw of $\tilde{p}_s$ on the two sides of the Dateline following the SO activity?

(2) Presumably, the answer to Question 1 is in the positive. How is this interannual spatial variation of $\tilde{p}_w$ maintained through the atmospheric hydrological processes and linked to the mechanism responsible for the seesaw of $\tilde{p}_s$?

The answer to the first question provides not only an insight into how the interannual variation of $\tilde{p}_s$ and $\tilde{p}_w$ are related to each other spatially, but also a basis upon which to search for a possible mechanism to couple these two interannual variations. On the other hand, some light may be shed on this mechanism by our answer to the second question.

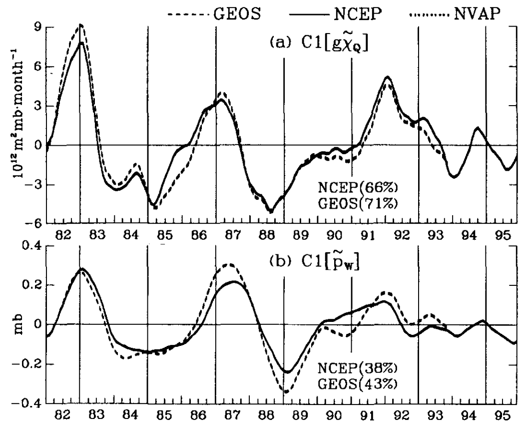

Fig. 7. Same as Fig. 4, except for (a) C1($\tilde{\chi}_Q$) and (b) C1($\tilde{p}_w$).

To answer the first question, we perform the EOF analyses of $\tilde{p}_s$; eigencoefficient (C1) time series and eigenvectors (E1) of the first leading eigenmodes are shown in Figs. 7, 8, respectively. The salient features of the first eigenmodes may be highlighted as follows.

(1) CI ($\tilde{p}_w$) ime series are highly correlated not only with each other, but also with the corresponding C1($\tilde{p}_s$) time series (Fig. 4d); correlation coefficients range from 0.7 to 0.8. The amplitudes of C1($\tilde{p}_w$)s are comparable to each other, but only about a half of those of C1($\tilde{p}_s$)s are.

(2) As revealed from E1($\tilde{p}_w$)s, the major centers of $\tilde{p}_s$(GEOS) and $\tilde{p}_w$(NCEP) anomalies are located slightly east of the Dateline and enclosed by the horseshoe-shaped $\tilde{p}_w$ anomalies of opposite sign. It may be inferred from the contrast between E1($\tilde{p}_w$)s and E1($\tilde{p}_s$) (Figs. 5d, h) that there are out-of-phase seesaws of $\tilde{p}_s$ and $\tilde{p}_w$ in the tropical Pacific (associated with the SO).

(3) Although the major anomalies of E1($\tilde{p}_w$)(NVAP) (Fig. 8e) are centered at the Dateline, the structure of this eigenvector resembles those of E1($\tilde{p}_w$)(GEOS) and E1($\tilde{p}_w$)(NCEP).

Since the interannual variation components depicted by the first eigenmodes of three $\tilde{p}_w$ datasets are so coherent, it would be unimaginable that the interannual variation component of water vapor pressure is not contained in the two assimilation datasets.

To understand the cause of the [$\tilde{p}_w$] interannual variation, one may argue that the global-mean water-vapor budget, i.e., $\partial[\tilde{p}_w]/\partial t = g[E-P]$, should be explored to illustrate the effect of $[E-P]$. With this approach, we actually face somewhat of a predicament: (1) There are no specifications of initial precipitation and evaporation, and no special constraint on the initial moisture condition in any assimilation system. The spinup caused partly by the initial imbalance between p_w and $E-P$ makes it unlikely for the hydrological processes contained in the assimilation data to reach a balance with the global-mean water vapor budget. (2) Even with a perfect assimilation dataset (in which this balance exists) available, we can only speculate about the link between the SO and the interannual variation in [$\tilde{p}_w$] through a comparison between the SO activity and temporal variation in either [$\tilde{p}_w$] or $[E-P]$. There is no way for us to disclose the link between the interannually spatial seesaws of $\tilde{p}_w$ and $\tilde{p}_w$ on the two sides of the Dateline in accordance with the SO activity. Nevertheless, this predicament may be resolved by a different approach. Recall that [$\tilde{p}_w$] is a global average of $\tilde{p}_w$. Conceivably, the cause of the interannual variation in [$\tilde{p}_w$] can be revealed through the mechanism causing the interannual variation of $\tilde{p}_w$ associated with the SO activity.

As shown previously, the interannual variation of $\tilde{p}_w$ occurs primarily in the central tropical Pacific. Thus, the hydrological processes that maintain this interannual variation may be illustrated through the analysis of the water-vapor budget:

$$\frac{\partial \tilde{p}_w}{\partial t} + g\nabla\cdot\tilde{Q} = g(E-P), \tag{1}$$

where

$$Q = \frac{1}{g}\int_o^{p_s} Vq\,\mathrm{d}p;$$

q, V, p_s and p are specific humidity, velocity vector, surface pressure and pressure, respectively. Water vapor flux Q may be split into rotational (Q_R) and divergent (Q_D) component, i.e., $Q = Q_R + Q_D$. Chen (1985) introduced the potential function of water vapor flux, χ_Q, so that divergence of water vapor flux and divergent water vapor flux can be expressed by:
$\nabla\cdot Q = \nabla\cdot Q_D = \nabla^2\chi_Q$ and $Q_D = \nabla\chi_Q$, respectively.

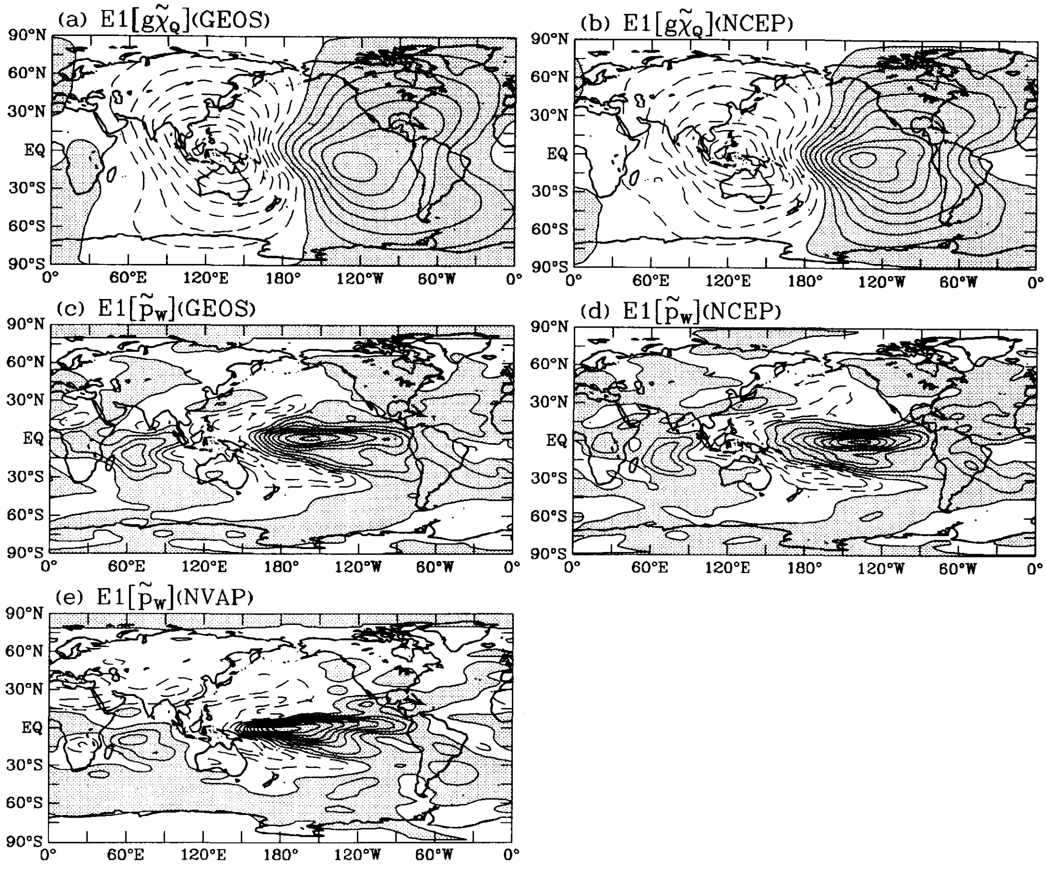

Fig. 8. Same as Fig. 5, except for (a) E1($\tilde{\chi}_Q$) and (b) E1($\tilde{p}_w$). Contour interval of every chart is 0.3.

Thus, eq. (1) may be written as

$$\frac{\partial \tilde{p}_w}{\partial t} + g\nabla^2 \tilde{\chi}_Q = g(E-P). \qquad (2)$$

Without any phase change, water vapor is only a passive atmospheric constituent, and Q_D is driven primarily by the lower-tropospheric divergent circulation. Since the global divergent circulation is often depicted with velocity potential χ, Q_D and χ_Q should have spatial structures similar to those of divergent wind vectors V_D and χ, respectively, in the lower troposphere.

Based upon the argument of the previous paragraph, χ_Q is a variable with which we can link the global divergent circulation to the regional source/sink of water vapor and to the maintenance of local water vapor. Following the last two sections, we perform the EOF analysis of $\tilde{\chi}_Q$; C1($\tilde{\chi}_Q$) and E1($\tilde{\chi}_Q$) are presented in Figs. 7, 8, respectively.

(1) The C1($\tilde{\chi}_Q$) time series are well correlated with C1[$\tilde{\chi}$(850 mb)] and C1($\tilde{p}_w$); correlation coefficients are around 0.8. The interannual variation of χ_Q represented by the first eigenmode follows closely those of $\tilde{\chi}$(850 mb) and $\tilde{p}_w$.

(2) The spatial structure of E1($\tilde{\chi}_Q$) resembles that of E1[$\tilde{\chi}$(850 mb)] (Figs. 5b, f). As inferred from the comparison between these two eigenvectors and E1($\tilde{p}_w$), it becomes clear that the lower-tropospheric divergent circulation converges water vapor toward (diverges water vapor out of) the central-eastern tropical Pacific region during the positive (negative) SO phase to maintain (deplete) water vapor over the positive (negative) maximum $\tilde{p}_w$ region.

The EOF analysis of $\tilde{\chi}_Q$ made here so far stresses only the local maintenance of the $\tilde{p}_w$ interannual variation through the anomalous convergence/divergence of water vapor flux. According to eq. (1) or (2), $(E-P)$ is an integrated part of the water vapor budget. What may be the role played by $g(E-P)$ in maintaining locally the interannual variation of $\tilde{p}_w$? We may be able to answer this question with the EOF analysis of $g(E-P)$. However, it was pointed out by Ramage and Hori (1981) and Deser and Wallace (1990) that the enhanced precipitation in the central tropical Pacific during the warm ENSO events is maintained by large-scale water-vapor flux convergence, instead of by local enhanced evaporation. Comparing $(E-P)$ and water vapor flux between the 1987 and 1988 winter with the two assimilation datasets, Mo and Higgins (1996) showed that their result supported this finding. In our EOF analysis, the first several leading eigenmodes of $g(E-P)$(GEOS) and $g\tilde{P}$(GEOS) highly resemble each other except for a spatial phase reversed in their eigenvectors. This resemblance indicates that only $\tilde{P}$ instead of $(E-P)$, is a vital variable to the interannual variation of atmospheric hydrological processes. Since Kalany et al. (1996) cautioned about the quality of P(NCEP), we thus focus our analysis only on P(GEOS). The assimilation precipitation data may contain significant model bias. We thus include the EOF analysis of P(GPCP) for verification. Results are presented in Fig. 9. The C1 time series of $\tilde{P}$(GEOS) and $\tilde{P}$(GPCP) (with amplitudes of about $0.5 \sim 1$ mm day^{-1}) are highly correlated with C1($\tilde{p}_w$) and C1(χ_Q) time series of the two assimilation data. The spatial structure of E1(P)s exhibits a predominant anomaly center in the central-eastern tropical Pacific as shown by Ropelewski and Halpert (1987). Note that precipitation is a sink of atmospheric water vapor. The coherent structure of E($\tilde{p}_w$) and E1($\tilde{P}$) indicates that water vapor converged toward the $\tilde{p}_w$ anomaly center during the warm ENSO events may be removed by precipitation.

Results of the EOF analyses of atmospheric mass, global divergent circulation and hydrological processes obtained in this study are summarized in the schematic diagrams shown in Fig. 10. We shall use these diagrams to answer the 2nd question posed previously. During the *positive* SO phase (Fig. 10a), the warm SST anomalies in the central-eastern tropical Pacific may induce the anomalous east-west Walker circulation straddling the Dateline (Fig. 5c, g); the upward (downward) branch of this anomalous circulation is located east (west) of 180°, as indicated by solid arrows. This anomalous circulation thus converges (diverges) water vapor toward (out of) the center — eastern (western) tropical Pacific to enhance (suppress) cumulus convection. The latent heat released by convection [as implicated by $[(E-P)>0]$ is fed back to maintain the anomalous east-west Walker circulation. As indicated in Fig. 10a, this anomalous circulation accumulates airmass by its downward branch over the western tropical Pacific and depletes airmass by its upward branch over the central-eastern tropical Pacific. The entire situation depicted by Fig. 10a is reversed during the negative SO phase (Fig. 10b). The local maintenance of the $\tilde{p}_w$ anomaly center west of the Dateline (Figs. 5d, h) and of the $\tilde{p}_w$ anomaly center east of the Dateline (Figs. 8c, d) is accomplished by the anomalous east-west Walker circulation. Consequently, the local signatures of $\tilde{p}_s$ and $\tilde{p}_w$ anomalies in the tropical Pacific are reflected in the coherent interannual increases (decreases) of the global-mean atmospheric mass and water vapor pressure associated with the positive (negative) SO phase.

5. Concluding remarks

The Southern Oscillation is an interannual seesaw of surface pressure (p_s) between the eastern Pacific and the western Pacific-Indian Ocean. Several questions concerning the interannual variation of atmospheric mass are raised in this study.

(1) Does the SO signal exist in the global atmospheric mass?

(2) If the SO signal exists in atmospheric mass, what is its local signature and how is it coupled between the eastern and western Pacific?

(3) Since dry atmospheric mass is conserved, the SO signal of global atmospheric mass should be caused by the interannual variation of moisture. How is this linked to local variations of atmospheric hydrological processes and of surface pressure?

To answer these three questions, we analyzed the p_s and moisture data generated by the GEOS-DAS for 1982–1993 and the NCEP-GDAS for

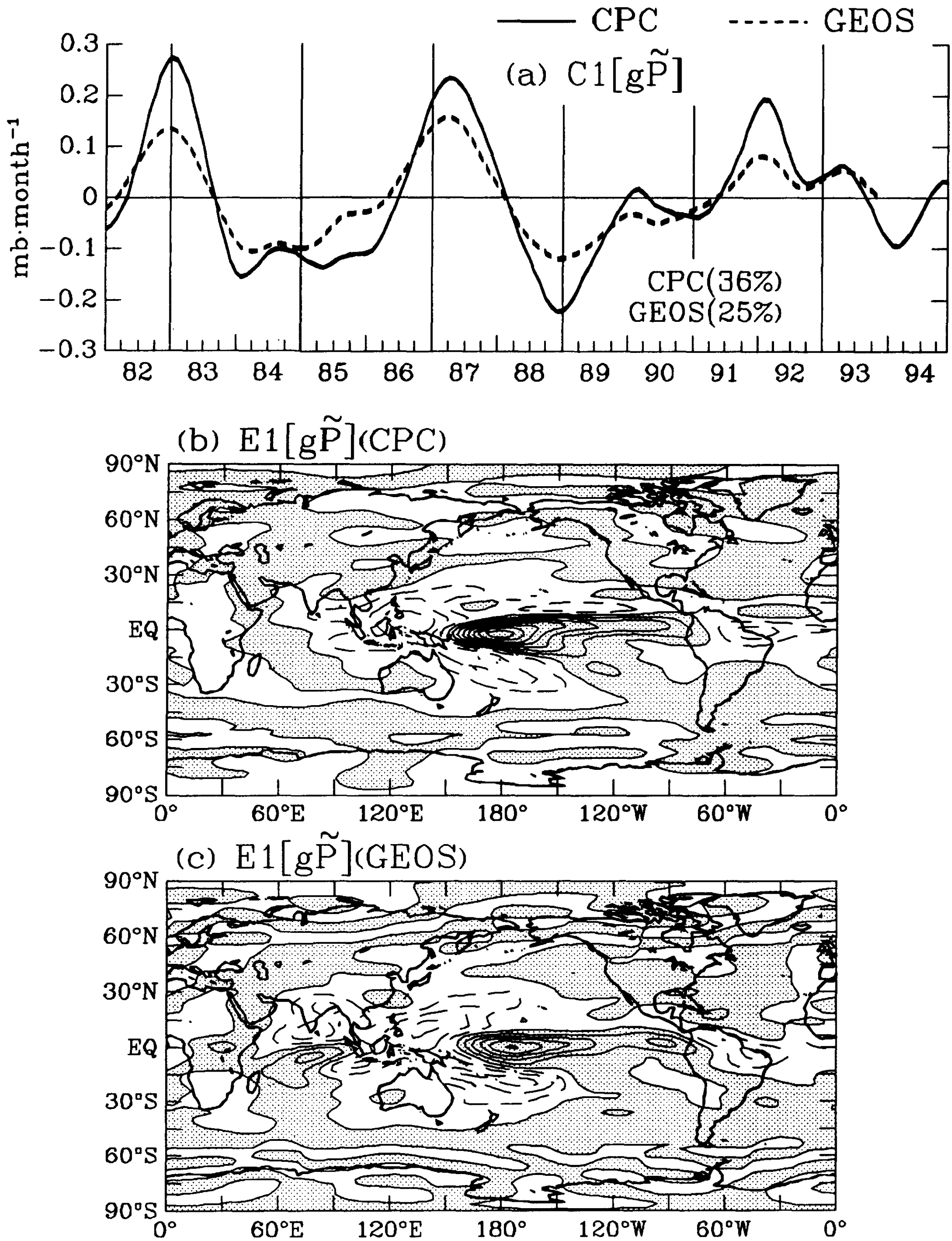

Fig. 9. Same as Figs. 4, 5, except $\tilde{P}$(GEOS) and $\tilde{P}$(CPC); "CPC" represents climate prediction center. Contour interval of E1 is 0.3.

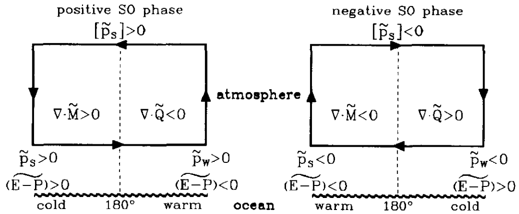

Fig. 10. Schematic diagrams of the anomalous east-west Walker circulation straddling the Dateline during (a) a positive SO phase and (b) a negative SO phase with $\tilde{p}_s$, $\tilde{p}_w$ and $(E-P)$ anomalies indicated on the bottom of the circulation. The direction of the anomalous east-west Walker circulation is indicated by arrows. The warm and cold SST anomalies during both the positive and negative SO phases over both the western and eastern tropical Pacific are also labeled underneath the zigzag line (which represents the sea surface). The vertically integrated mass and water vapor convergence (divergence) are represented by $\nabla\cdot\tilde{M}<0(\nabla\cdot\tilde{M}>0)$ and $\nabla\cdot\tilde{Q}<0(\nabla\cdot\tilde{Q}>0)$, respectively. Note that $\nabla\cdot\tilde{M}$ is defined in terms of the surface pressure tendency equation: $\partial p_s/\partial t = -g\nabla\cdot M(= -g\int_o^{p_s} \nabla\cdot v dp)$.

1982–1995, as well as the divergent circulation and atmospheric hydrological processes depicted by these two datasets. Because of the assimilation system bias, our analyses of water vapor pressure and precipitation also included the 1987–1992 precipitable water and precipitation generated by the NASA Water Vapor Project (NVAP) and the NOAA Global Precipitation Climatology Project (GPCP) of the Climate Prediction Center for comparison. The major findings and answers to the three questions are as follows.

(1) A clear SO signal emerges from time series of the globally-averaged low-pass filtered (with a 18-month cut-off time) surface pressure, $[\tilde{p}_s]$. The $[\tilde{p}_s]$ time series is coincident with the $\tilde{\text{SST}}$ (NINO3) index, with correlation coefficients between the time series of these two indices being 0.85 for GEOS and 0.82 for NCEP, respectively.

(2) The interannual increase (decrease) of the global atmospheric mass results from the local signature of the surface pressure change, displaying an increase (decrease) over the western Pacific and an opposite change over the central-eastern Pacific. This contrast of the east-west surface pressure change is maintained by an anomalous Walker circulation that is driven by enhanced or suppressed convection over the central-eastern Pacific.

(3) The interannual variation of globally-integrated water-vapor pressure, $[\tilde{p}_w]$, is coherent with that of $[\tilde{p}_w]$ for the following reason: water vapor is converged (diverged) toward (out of) the central-eastern tropical Pacific to maintain (suppress) cumulus convection there during the positive (negative) SO phase, and in turn maintains the east-west Walker circulation which sustains the major positive (negative) $\tilde{p}_s$ center west of the Dateline.

The findings of this study may not be fully accepted without addressing the following concerns.

(1) In view of having only limited SO phases available for this study, the results obtained here may be considered tentative. The NCEP/NCAR reanalysis for 1957–1996 was scheduled to be available by the end of 1997. The completion of this reanalysis data may allow confirmation of the tentative conclusions of this study.

(2) Because of the possible model bias in the moisture fields of the two reanalysis datasets, the NVAP precipitable water data were applied for verification of our analysis; variations of $[\tilde{p}_w]s$ and spatial structures of $\tilde{p}_w s$ generated from the three data sources are comparable. This comparison suggests that the interannual variation of $\tilde{p}_w$ may be depicted by the reanalysis data. On the other hand, the short-period of the NVAP precipitable water provides only a limited verification.

6. Acknowledgements

This study is supported by the NSF Grant ATM-9416954 and the NASA Grant NAG5-2930. Comments and suggestions offered by the two reviewers of the original version of this paper are helpful in clarifying some issues addressed in this paper. The typing support provided by Mrs. Reatha Diedrichs and the editing assistance by Mrs. Susan Carr are highly appreciated.

7. Appendix

In this study, velocity potential (χ), which is a mass flux function, is used (rather than horizontal wind vectors) to depict the global divergent circulation on a horizontal plane. Although the east-west Walker circulation may be portrayed in terms of vectors (u_D, ω) on a longitudinal-height plane, it would be more proper for us to link this circulation to velocity potential; this is done by introducing a mass flux function χ_m [as proposed by Newell et al. (1974)] to construct the east-west Walker circulation. By neglecting meridional divergence, the continuity equation averaged over a latitudinal zone between latitudes ϕ_1 and ϕ_2 may be approximated as,

$$\frac{\partial \hat{u}_D}{\partial x}+\frac{\partial \hat{\omega}}{\partial p}=0,$$

where u_D is zonal divergent wind and

$$(\hat{\ })=\frac{1}{(\phi_2-\phi_1)}\int_{\phi 1}^{\phi_2}(\ )\,d\phi.$$

Based upon this approximated continuity equation, we introduce a mass flux function

$$\psi_m=\int_p^{p_0}\hat{u}_D\,dp,$$

where $p_o=1000$ mb. A positive (negative) value of ψ_m represents a counterclockwise (clockwise) circulation. As revealed from our analysis (not shown) with the GEOS and NCEP data, the east-west Walker circulation portrayed with ψ_m resembles that portrayed with the employing vectors($\hat{u}_D$, $\hat{\omega}$).

REFERENCES

Berlage, H. P. 1957. Fluctuations in the general atmospheric circulation of more than one year, their nature and prognostic value. *K. Ned. Meteor. Inst., Meded. Verb.* **69**, 1–52.

Chen, W. Y. 1982. Assessment of Southern Oscillation sea level pressure indices. *Mon. Wea. Rev.* **110**, 800–807.

Chen, T.-C. 1985. Global water vapor flux and maintenance during FGGE. *Mon. Wea. Rev.* **113**, 1801–1819.

Chen, T.-C., Tribbia, J. J. and Yen, M.-C. 1996. Interannual variation of global atmospheric angular momentum. *J. Atmos. Sci.* **53**, 2852–2857.

Chen, T.-C., Chen, J.-M., Schubert, S. and Takacs, L. L. 1997. Seasonal variation of global surface pressure and water vapor. *Tellus*, in press.

Deser, C. and Wallace, J. M. 1990. Large scale atmospheric circulation features of warm and cold episodes in the tropical Pacific. *J. Climate* **3**, 1254–1281.

Holton, J. R. 1992. *An introduction to dynamic meteorology*, 3rd edition. Academic Press (ISBN 0–12–354355-X), 511 pp.

Kalnay, E. and Jenne, R. 1991. Summary of the NMC/NCAR reanalysis workshop of April 1991. *Bull. Amer. Meteor. Soc.* **72**, 1897–1904.

Kalnay, E., Kanamitsu, M., Kistler, R., Collins, W., Deaven, D., Gandin, L., Iredell, M., Saha, S., White, G., Woollen, J., Zhu, Y., Chelliah, M., Edisuzaki, W., Higgins, W., Janowiak, J., Mo, K. C., Ropelewski, C., Wang, J., Leetmaa, A., Reynolds, R., Jenne, Roy and Joseph, Dennis. 1996. The NCEP/NCAR 40-year reanalysis project. *Bull. Amer. Meteor. Soc.* **77**, 473–471.

Karoly, D. J., 1989. Southern Hemisphere circulation features associated with El Niño-Southern Oscillation. *J. Climate* **2**, 1239–12523.

Kousky, V. E., Kagano, M. T. and Cavaleant, I. F. 1984. A review of the Southern Oscillation: Ocean-atmospheric circulation changes and related rainfall anomalies. *Tellus* **36A**, 490–504.

Mo, K. C. and Ghil, M. 1987. Statistics and dynamics of persistent anomalies. *J. Atmos. Sci.* **44**, 877–901.

Mo, K. E. and Higgins, R. W. 1996. Large-scale atmospheric moisture transport as evaluated in the NCEP/NCAR and the NASA/DAO reanalyses. *J. Climate* **9**, 1531–1545.

Newell, R. E., Kidson, J. W., Vincent, D. J. and Boer, G. J. 1974. *The general circulation of the tropical atmosphere.* MIT Press, 370 pp. (ISBN 0–26–14029–9).

Ramage, C. S. and Hori, A. M. 1981. Meteorological aspects of El Niño. *Mon. Wea. Rev.* **109**, 1827–1825.

Randel, D. L., vanderHarr, T. H., Ringerud, M. A., Reinke, D. L., Stephens, G. L., Combs, C. L., Greenwald, T. J. and Wittmeyer, I. L. 1995. An introduction to the NASA Water Vapor Project Data Set (NVAP). *Technical Report to NASA Headquarters*, under contract NASW-4715 (available through ftp ncardata.ucar.edu-cd/datasets/ds722.0).

Ropelewski, C. F. and Halpert, M. S. 1987. Global and regional scale precipitation associated with the El Niño. *Mon. Wea. Rev.* **115**, 1589–1610.

Schubert, S. D., Pfaendtner, J. and Rood, R. 1993. An assimilation data set for Earth Science application. *Bull. Amer. Meteor. Soc.* **74**, 2331–2342.

Trenberth, K. E. and Shea, D. J. 1987. On the evolution of the Southern Oscillation. *Mon. Wea. Rev.* **115,** 3078–3096.

Trenberth, K. E., Christy, J. R. and Olson, J. G. 1987. Global atmospheric mass, surface pressure, and water vapor variations. *J. Geophys. Res.* **92**, no. D12, 14, 815–14, 826.

Trenberth, K. E. and Olson, J. G. 1988. An evaluation and intercomparison of global analyses from NMC and ECMWF. *Bull. Amer. Meteor. Soc.* **69**, 1047–1057.

Van den Dool, H. and Saha, S. 1993. Seasonal redistribution and conservation of atmospheric mass in a general circulation model. *J. Climate* **6**, 22–30.

Walker, G. T. 1923. Correlation in seasonal variations of weather. VIII. A. preliminary study of world weather. *Mem. Indian Meteor. Dep.* **24**, 75–131.

Walker, G. T. 1924. Correlation in seasonal variations of weather IX. A further study of world weather. *Mem. Indian Meteorol. Dep.* **24**, 275–332.

Walker, G. T. 1928. World weather (III). *Mem. R. Meteorol. Soc.* **2**, 97–106.

Walker, G. T. and Bliss, E. W. 1930. World weather (IV). *Mem. R. Meteorol. Soc.* **3**, 81–85.

Walker, G. T. and Bliss, E. W. 1932. World weather (V). *Mem. R. Meteorol. Soc.* **4**, 53–84.

Walker, G. T. and Bliss, E. W. 1937. World weather (VI). *Mem. R. Meteorol. Soc.* **4**, 119–139.

Wallace, J. M. and Gutzler, D. S. 1981. Teleconnections in the geopotential height field during the Northern Hemisphere winter. *Mon. Wea. Rev.* **109**, 784–812.

World Climate Research Program, 1992. *CLIVAR A study of climate variability and predictability*, 32 pp, available from World Meteorological Organization, Geneva, Switzerland.

Xie, P. and Arkin, P. A. 1997. Global precipitation: a 17-year monthly analysis based upon gauge observations, satellite estimates and numerical model outputs. *Bull. Amer. Meteor. Soc.*, in press.